Acta Materialia 261 (2023) 119348

Contents lists available at ScienceDirect

Acta Materialia

journal homepage: www.elsevier.com/locate/actamat

Full length article

Stable and metastable rare-earth-free permanent magnets from a database of predicted crystal structures

Alena Vishina *, Olle Eriksson, Heike C. Herper

Department of Physics and Astronomy, Uppsala University, Box 516, SE-75120, Uppsala, Sweden

ARTICLE INFO

Keywords:
Permanent magnets
Rare-earth-free
High-throughput
DFT
Neural networks
Structure prediction

ABSTRACT

With the recent developments in crystal structure prediction, databases of new (not previously synthesized) materials are being created. One of these databases contains more than a million entries with the distance to the Convex Hull predicted by crystal-graph attention networks. Hence, stable and metastable materials can be extracted and then investigated for any desired properties. A high-throughput and data-mining approach we previously developed to search for rare-earth-free permanent magnets was applied to these compounds. As a result, four promising candidates for novel rare-earth-free permanent magnets were discovered with high magnetization, high uniaxial magnetocrystalline anisotropy, and high Curie temperature - Ta_3ZnFe_8, $AlFe_2$, Co_3Ni_2, and Fe_3Ge. The materials were investigated in more detail and all were verified to be dynamically stable.

1. Introduction

One of the pieces in the work against climate change is the transition to renewable energy sources (e.g. wind power) and sustainable transportation (electric vehicles). The resulting increased demand for high-performance permanent magnets (PMs) drives the research into new magnetic materials. All the PMs used in wind-turbine end electric vehicle engines are based on rare-earth (RE) elements [1], many of which are on the list of critical raw materials [2]. They are subject to high supply risks, are not recycled efficiently, and are often mined with a high strain on the environment. Hence, there is a growing interest in finding high-performance PMs that are free from or contain smaller amounts of RE elements. Some companies have recently announced the transition to RE-free PMs as one of their goals [3].

Many approaches are developed to solve this problem. Considerable work is being done on improving the magnetic properties of known materials with high magnetocrystalline anisotropy, e.g. MnBi [4,5] and MnAl [6,7], $\alpha'' - Fe_{16}N_2$ [8,9]. Various geometries are tried, such as nanostructures [10–13], thin films [14,15], nanofibers [16], and many more [17,18].

We have previously developed [19] and used [20,21] a high-throughput computational approach to the search for RE-free PMs. However, in all the investigations, we were filtering through the materials of the Inorganic Crystal Structure Database (ICSD) [22]. In this database, all entries have been previously reported from experiment. Recently, some sieving through the ICSD database were performed by other researchers as well [23]. However, looking for new materials (which have never been synthesized before) can provide valuable guidance for future experiments and can be quite useful in the search for novel RE-free PMs.

As computational materials science, particularly approaches based on the ab-initio theory that relies on density functional theory (DFT), can investigate multiple combinations of elements of the Periodic Table in various geometrical arrangements with more freedom than the experiment, there is an increasing interest in stable and metastable crystal structure prediction. This way, theory can guide the experiment by suggesting the plausible new materials that are worthwhile of a synthesis attempt. Different methods have been developed in this quest, such as evolutionary techniques [24–27], deep-learning [28], machine-learning [29], and others [30–32]. Moreover, a combination of experimental approaches with computational techniques (e.g. machine-learning) was used in the search for new stable and metastable magnetic materials in [33–35].

A database of new (experimentally unknown) crystal structures was recently created using the new graph neural network approach and machine learning [36,37]. A large space of almost 1 billion crystalline compounds was explored by scanning the composition space for various crystal structure prototypes. This resulted in a data set of DFT calculations for about 2.6 million crystal structures [38]. Most importantly, the data for each material contains the distance to the convex hull of thermodynamic stability predicted by the crystal-graph attention network [37]. It can be used to evaluate if the material

* Corresponding author.
E-mail address: alena.vishina@physics.uu.se (A. Vishina).

https://doi.org/10.1016/j.actamat.2023.119348
Received 10 July 2023; Received in revised form 30 August 2023; Accepted 13 September 2023
Available online 20 September 2023

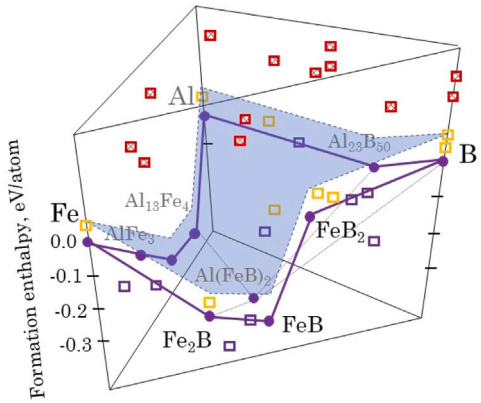

Fig. 1. A schematic image of a convex hull for Fe-B-Al systems. Purple circles denote stable materials (their formation enthalpies were taken from the Materials Project [41]) and form the convex hull. The surface 50 meV above it limits the metastable materials (which can still be synthesized). Squares symbolize the result of structure generation - blue (below hull) and orange (less than 50 meV above it) will pass through our filters, the red will not be considered further. (For interpretation of the references to color in this figure legend, the reader is referred to the web version of this article.)

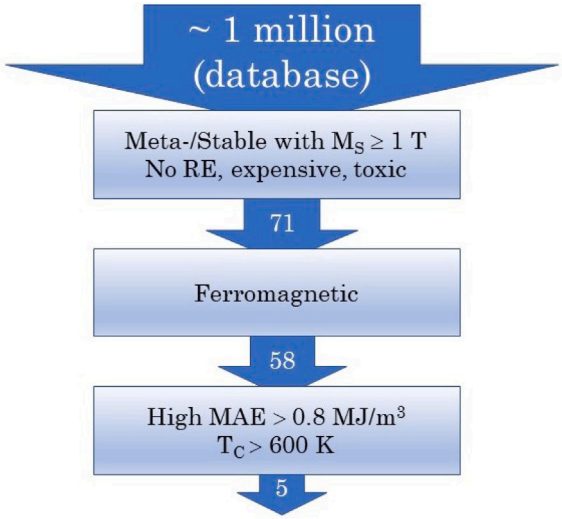

Fig. 2. The steps of the high-throughput search with the number of systems remaining at each step. (For interpretation of the references to color in this figure legend, the reader is referred to the web version of this article.)

can be synthesized experimentally. All the materials are geometrically optimized with DFT.

In this work, we will apply our high-throughput filtering technique reported in Refs. [19–21] to the crystal structures predicted in [37]. Promising candidates for high-performance permanent magnets found as the result will be further discussed and tested for dynamical stability.

2. High-throughput filtering and further calculations

The crystal structure database contains three separate data sets [38]. According to the authors of Ref. [38], the first one is quite biased due to the lack of structural and chemical diversity in the available data [36]. This issue was later overcome, resulting in creation of two additional data sets [37] with a reduced mean absolute error in the distance to the convex hull. In our search, we will consider the latter two data sets only.

As we are interested in metastable and stable materials, which makes them possible to be synthesized experimentally, the first filtering criterion we employ is the distance to the convex hull. We select those entries where the distance is less than 50 meV, which makes them likely to be synthesized [39,40]. Fig. 1 illustrates our selection.

The database created by machine-learning-assisted exploration of the materials space [37,38] already contains the magnetic moments of the crystal structures included in it. However, those magnetic moments were obtained starting with the ferromagnetic (FM) initial orientation of the moments. Hence, we first filter through the database for the materials with sufficiently high saturation magnetization ($M_S \gtrsim 1$ T). Next, however, we need to make sure that the FM state is the ground state of the system. Calculations are performed here for the FM initial configurations of the spins (assumed when the database was produced) and several possible anti-ferromagnetic (AFM) orientations of the magnetic moments to see which state is more stable. We have also excluded all the materials with RE-elements, as well as the elements that are expensive, difficult to work with experimentally, and radio-active (Au, Tc, Ru, Hg, Pt, As, Pd, Ir, Rh, Tl, Os, Pu, Th, Ag). Out of about a million compounds in the database, excluding all the unwanted elements, we were left with 71 stable and metastable materials with $M_S \gtrsim 1$ T. Checking for the magnetic state, we found some to be AFM. Here, we also excluded systems where the FM state was energetically very close to an AFM configuration ($\Delta E_{AFM-FM} < 10$ meV). All the materials can be found in the *Appendix* A, (Table 2). For the systems that were found to be FM, we further calculated the magnetic anisotropy energy (MAE) and Curie temperature (see *Methods* section for further details). Only those with MAE > 0.8 MJ/m^3 and T_C > 600 K were investigated further. For the high-throughput step, MAE is calculated as the difference in total energy between the states with the magnetization directed along and perpendicular to the c-axis, as the same criteria are applied for a large number of systems. However, for the systems of interest, additional calculations are then performed for spin axes pointing in several directions. The procedure is schematically shown in Fig. 2.

3. Results

Materials with high enough saturation magnetization, MAE, and Curie temperatures can be further explored with respect to similar phases, stability, and existing compounds. Additional magnetocrystalline anisotropy analysis was also performed for the promising compounds to see the change in the total energy with different orientations of the spin axes. The details can be found in Appendix D.

3.1. Ta_3ZnFe_8

Ta_3ZnFe_8 found in the database has M_S = 0.94 T, MAE = 3.02 MJ/m^3, and T_C = 630 K with a zero distance to the convex hull and formation energy of −163 meV/at. The unit cell with space group number 160 is shown in Fig. 3. Neither Ta_3ZnFe_8 nor any other ternaries combining Ta, Zn, and Fe are reported either experimentally or theoretically (as per ICSD [22] and The Materials Project [41]). According to the phase diagram, the solubility of Ta in Fe is 17% at 600 °C, however, it increases with temperature up to 28% for 900 °C [42], which is about the ratio of Ta and Fe in Ta_3ZnFe_8 (not considering Zn). The necessary solubility of Zn in Fe can be reached around 1100 °C, according to [43]. Only two Ta-Zn phases, namely Ta_6Zn_7 and $TaZn_2$, have been reported [44].

3.2. Ga_2Fe_6B

Ga_2Fe_6B was found to be a FM compound with M_S = 1.49 T, MAE = 0.80 MJ/m^3, and T_C = 1170 K. The material has hexagonal crystal structure with space group number 189. The distance above the convex hull is 29 meV/at with the formation energy of −173 meV/at against the decomposition into $GaFe_3$, Fe_2B, and Ga_3Fe. Again, no ternaries with Ga, Fe, and B are in either ICSD or the Materials Project. The

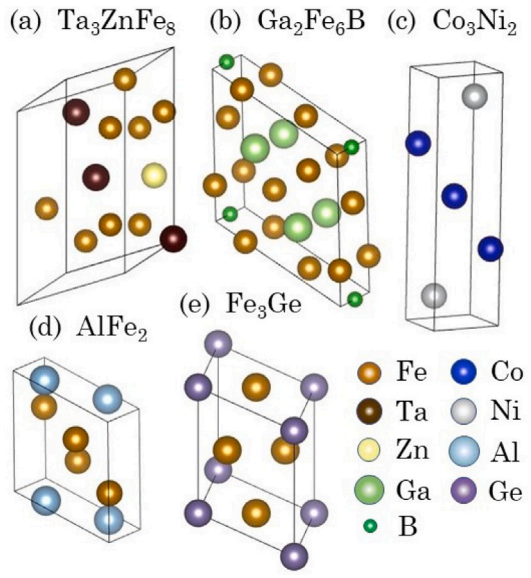

Fig. 3. The unit cell of (a) Ta_3ZnFe_8, (b) Ga_2Fe_6B, (c) Co_3Ni_2, (d) $AlFe_2$, and (e) Fe_3Ge. The c-axis is pointing upwards. (For interpretation of the references to color in this figure legend, the reader is referred to the web version of this article.)

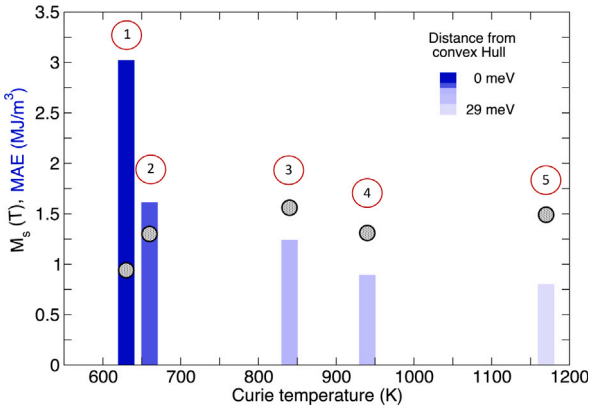

Fig. 4. A summary of magnetic properties and the distances to the convex hull for the five most promising stable and metastable systems derived from the HT search: ① (SG 160) Ta_3ZnFe_8, ② (SG 187) $AlFe_2$, ③ (SG 139) Fe_3Ge, ④ (SG 166) Co_3Ni_2 ⑤ (SG 189) Ga_2Fe_6B The bars give the values of MAE while their color code denotes the distance from the convex Hull. The gray circles mark the saturation magnetization. (For interpretation of the references to color in this figure legend, the reader is referred to the web version of this article.)

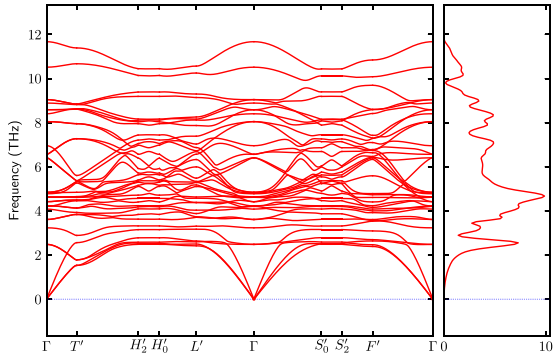

Fig. 5. Calculated phonon band dispersion (left) and vibrational density of states (right) for Ta_3ZnFe_8. (For interpretation of the references to color in this figure legend, the reader is referred to the web version of this article.)

crystal structure of Ga_2Fe_6B is shown in Fig. 3. The low-temperature melting point of Ga can be problematic (29.76 °C). However, according to the phase diagram, a high-temperature phase $Fe_{0.75}Ga_{0.25}$ exists between 590 and 730 °C [45].

As we can see in Appendix D, the more detailed investigation of MAE shows that in Ga_2Fe_6B the plane formed by c and b-axes is an easy magnetization plane.

3.3. $AlFe_2$

Another structure remaining after the high-throughput filtering is $AlFe_2$ with M_S = 1.30 T, MAE = 1.61 MJ/m^3, and T_C = 660 K (Fig. 3). It should crystallize in space group 187 with the energy of 11 meV/at above the Convex Hull and has a formation energy of −230 meV/at. According to the database, another phase of $AlFe_2$ will form under the ambient conditions, namely space group 191. There are no compounds with $AlFe_2$ composition within the previously synthesized materials of ICSD. There are two such systems in the Materials Project, not with the same structure, however. On top of that, there are many synthesized binaries of Al and Fe. It is worth mentioning here, that all the data from the Materials Project as well as all data from AFLOW [46] were used to construct the dataset for machine learning [36]. Hence, all the above-mentioned binaries are included in the convex hull.

3.4. Co_3Ni_2

We would also like to highlight Co_3Ni_2. It has a slightly lower magnetic anisotropy of 0.89 MJ/m^3 than that required for a high-performance PM. However, the magnetization of with M_S = 1.31 T, and high Curie temperature T_C = 940 K can make it a promising gap magnet. Its space group number is 166. Energy above the convex hull is 25 meV/at (decomposition into Co_3Ni and $CoNi_3$) with the formation energy of 2 meV/at. We could find neither synthesized nor theoretically predicted material with the chemical formula Co_3Ni_2 (Fig. 3), however, there exist several binaries of Co and Ni. One of the complications here might be the fact that Co-Ni exists for the whole temperature range as solid solution [47].

3.5. Fe_3Ge

The last material we report on is Fe_3Ge. Its magnetic characteristics are M_S = 1.56 T, MAE = 1.24 MJ/m^3, and T_C = 840 K, the unit cell is shown in Fig. 3. It has tetragonal crystal structure (139), a distance to the Convex Hull of 24 meV/at and a formation energy of −76 meV/at. Under normal conditions, another crystal structure of Fe_3Ge will be formed, the stable cubic structure (space group 225). However, several crystal structures of Fe_3Ge were observed experimentally, though none in the same symmetry group as the one given here. There are many investigations into magnetic properties of various forms of Fe_3Ge, e.g. [48–50]. As the distance from the convex hull for the desired material is small, one of the possible solutions for obtaining the correct crystal structure might be growing it on a suitable substrate.

4. Discussion and conclusions

With skyrocketing interest in machine-learning methods, there is a constant development in crystal structure prediction, resulting in a huge number of new materials. The main interest lies, however, in finding the compounds that can be further produced experimentally. Here we have filtered through about a million entries of the database containing new (not previously synthesized) materials, looking for stable and metastable compounds (as determined by the distance to the Convex Hull) that can be promising candidates for RE-free PMs [38]. As mentioned previously, we investigated two of the more reliable (according to the authors [37]) datasets.

As the initial magnetic state in the database was assumed to be FM, we had to check for the stable magnetic ground state configuration, finding several systems to prefer the AFM state. To see the full list of materials we investigated (with $M_S \gtrsim 1\ T$ reported in the database), see Appendix A, (Table 2). The list also contains materials discarded on other bases, such as low or in-plane magnetocrystalline anisotropy and non-collinear magnetic structures at elevated temperatures.

Five materials were found to be interesting candidate phases, their properties are shown in Fig. 4 and listed in Appendix A, (Table 1). One of them, Ta_3ZnFe_8, is stable (with zero distance to the convex hull), while the other four are metastable (distance to the hull below 50 meV).

The ratio between magnetization and MAE is an important characteristic of a permanent magnet, as it determines the hardness κ of a magnet and $\kappa \geq 1$ is needed for a hard magnet in order to resist the self-demagnetization [51]. Two of the systems, Ta_3ZnFe_8 (magnetic hardness parameter $\kappa = 2.07$) and $AlFe_2$ ($\kappa = 1.09$), have significantly higher coercivity.

As we demonstrated in Appendix D, it is important, especially in the case of crystal structures generated theoretically, to keep in mind that calculating magnetocrystalline anisotropy energy as a difference in the total energy for the spins aligned along the *c*-axis and perpendicular to it might require an additional investigation. In the case of Ga_2Fe_6B, the plane formed by the *b*- and *c*- axes was found to be an easy plane.

We also looked into the origin of high magnetocrystalline anisotropy in the five materials discovered, for details see *Appendix* B. As expected, the high MAE in Ta_3ZnFe_8 originates in the *5d*-element. Iron sources high values of anisotropy in the other three Fe-base materials. The key element in Co_3Ni_2 is cobalt.

All five systems, with their high Curie temperatures, if synthesized, can be promising permanent magnets. Ta_3ZnFe_8, with its magnetization slightly lower than 1 T but extremely high MAE, can be used as a gap material. As several crystal structures of Fe_3Ge have been discovered experimentally, however, it might be difficult to obtain the necessary phase experimentally.

As the materials of the database were predicted theoretically, we calculated the phonon dispersions for the five candidate materials, to test their dynamic stability. The resulting phonon band dispersions and vibrational densities of states are shown in Fig. 5 for Ta_3ZnFe_8 and in *Appendix* C Fig. 8 for the other four compounds. We can see the absence of imaginary frequencies in the phonon dispersion for all five materials, hence they are dynamically stable.

In conclusion, in the current investigation, we bridged the modern-day structure generation techniques and our high-throughput approach to the search for high-performance permanent magnets. The possibility of synthesizing these materials was one of the search criteria, as we considered both their distance to the Convex Hull and their dynamic stability. We suggest that the four candidate phases, Ta_3ZnFe_8, $AlFe_2$, Co_3Ni_2, and Fe_3Ge, can be interesting materials to consider for an experimental investigation.

5. Methods

When the stable and meta-stable materials with high magnetic moment were filtered from the database, the energies of the states with FM and several AFM initial magnetic configurations were calculated using Vienna Ab Initio Simulation Package (VASP) [52,53] within the Projector Augmented Wave (PAW) method [54]. Generalized Gradient Approximation (GGA) in Perdew, Burke, and Ernzerhof (PBE) form [55] was employed. Only systems with FM ground state were kept.

Full-potential linear muffin-tin orbital method (FP-LMTO), including spin–orbit interaction as implemented in the RSPt code [56,57], with the PBE functional [55] for exchange and correlation was used further. Tetrahedron method with Blöchl correction for the Brillouin zone integration [58,59] was employed. The initial magnetic state for each compound was set to be ferromagnetic (FM). In the high-throughput step, magnetic anisotropy energy (MAE) was calculated as the energy difference $\Delta E = E^{pl} - E^{c}$ between the states with the magnetization directed along (E^c) and perpendicular (E^{pl}) to the *c*-axis. A positive sign corresponds to the uniaxial magnetic anisotropy. The converged k-point Monkhorst–Pack meshes [60] 20 × 20 × 20 were used for the calculations.

The Curie temperature and magnetic state at higher temperatures were determined using Metropolis Monte Carlo (MC) and Atomistic Spin Dynamics (ASD) simulations, as implemented within the Uppsala Atomistic Spin Dynamics (UppASD) software [61]. The simulations were performed with a 25 × 25 × 25 supercell with periodic boundary conditions. Exchange parameters were calculated with the RSPt code within the first seven coordination shells [62–64].

The magnetic hardness parameter was calculated as $\kappa = \sqrt{\Delta E/\mu_0 M_S^2}$ [65], where ΔE is MAE, M_S is saturation magnetization and μ_0 is the vacuum permeability.

PHONOPY code [66] and a finite displacement method were used to produce phonon dispersion curves. 3 × 3 × 3 supercell and the displacement of 0.01 Å was employed to calculate forces with VASP. Crystal structures were relaxed with respect to the ions positions but not the cell shape or volume.

In addition, the Sumo package [67] and VESTA code [68] were utilized for visualization.

CRediT authorship contribution statement

Alena Vishina: Initiated the research, Performed the high-throughput search & initial data analysis, Drafted the manuscript, Review & edited, Contributed to discussions & analysed the data. **Olle Eriksson:** Initiated the research, Review & edited, Contributed to discussions & analysed the data. **Heike C. Herper:** Initiated the research, Review & edited, Contributed to discussions & analysed the data.

Declaration of competing interest

The authors declare that they have no known competing financial interests or personal relationships that could have appeared to influence the work reported in this paper.

Acknowledgments

The authors would like to acknowledge the support of the Swedish Foundation for Strategic Research, the Swedish Research Council (VR), the Swedish Energy Agency, the Knut and Alice Wallenberg Foundation (KAW), STandUPP, eSSENCE, and the ERC (synergy grant FASTCORR, project 854843). The calculations were performed with the resources provided by the Swedish National Infrastructure for Computing (SNIC) and National Academic Infrastructure for Supercomputing in Sweden (NAISS) (SNIC 2022/5-338, SNIC 2021/1-36) and partially funded by the Swedish Research Council through grant agreement no. 2018-05973, and UPPMAX, Sweden (SNIC 2021/5-340).

Appendix A. Stable and metastable materials with the high magnetic moment found in the database

Five promising candidates were found as the result of the high-throughput search, their detailed information is given in Table 1. Distances to the convex hull and the formation energies are extracted from the database, magnetic moment, MAE, and T_C were calculated.

Some of the materials with magnetic moment close to or higher than 1.0 T (as found in the database) were then discarded due to either the non-FM ground state, low or planar MAE, or low Curie temperature. These materials are listed in Table 2 along with the calculated values of M_S, MAE, T_C, and the energy difference between the FM and AFM states. Note, that when a value was found to be below the required, other characteristics were not calculated.

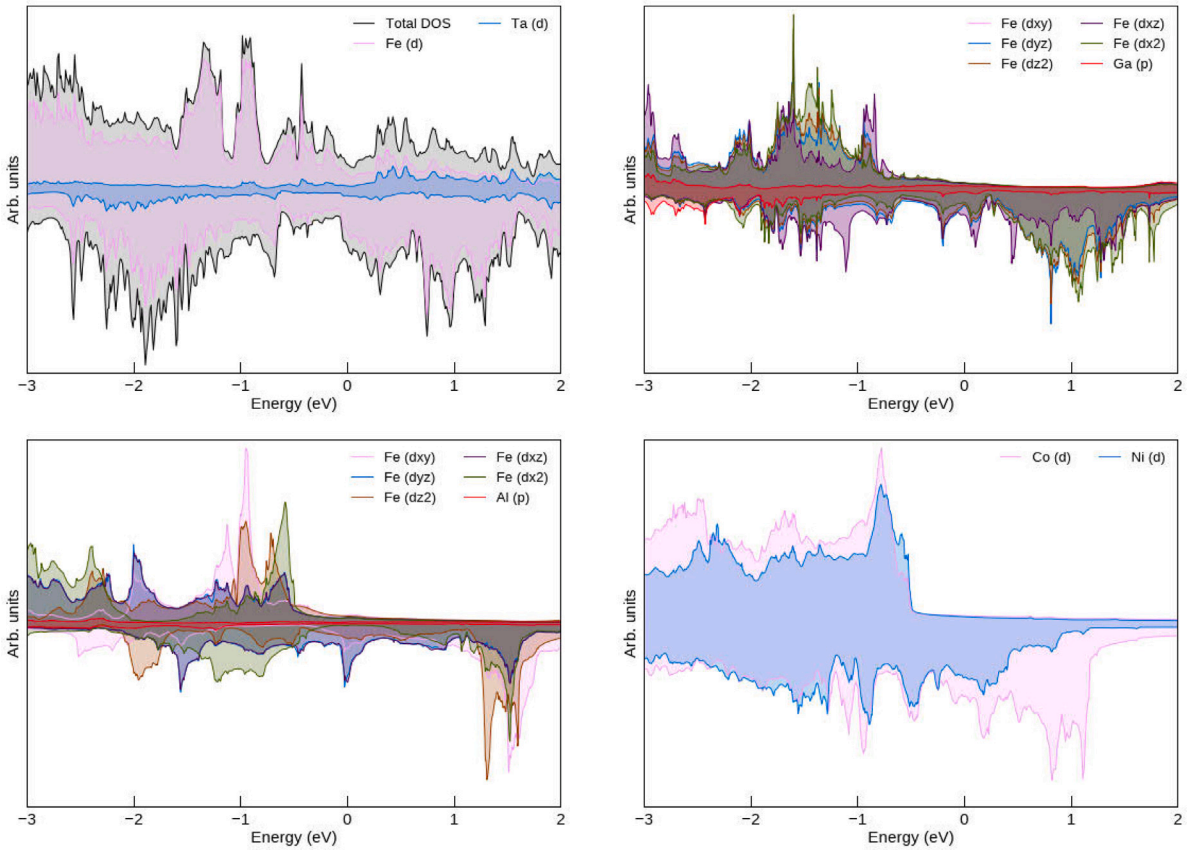

Fig. 6. Spin-polarized DOS (without SOC interaction) of Ta_3ZnFe_8 (top left panel), Ga_2Fe_6B (top right), $AlFe_2$ (bottom left), and Co_3Ni_2 (bottom right). For some of the materials, it is separated into the contributions from the $d_{x^2-y^2}$ and d_{z^2} (e_g set); d_{xy}, d_{yz}, and d_{xz} (t_{2g} set) orbitals. Fermi energy is set at zero. (For interpretation of the references to color in this figure legend, the reader is referred to the web version of this article.)

Table 1
Promising stable and metastable systems with their point symmetry group, saturation magnetization, MAE, Curie temperature, distance to the convex hull (a positive value means the material is above Hull), formation energy (negative sign points to table structures), and magnetic hardness coefficient.

Material	Symmetry group	M_S	MAE	T_C	Distance to Hull	Formation energy	κ
		T	MJ/m^3	K	meV	meV	
Ta_3ZnFe_8	160	0.94	3.02	630	0	−163	2.1
Ga_2Fe_6B	189	1.49	0.80	1170	29	−173	0.68
$AlFe_2$	187	1.30	1.61	660	11	−230	1.1
Co_3Ni_2	166	1.31	0.89	940	25	2	0.89
Fe_3Ge	139	1.56	1.24	840	24	−76	0.80

Appendix B. The origin of magnetic anisotropy in the promising compounds

Similar to our of previous works [20,21] and the analyses presented in Refs. [69–74], to determine the origin of MAE we can calculate the spin–orbit coupling energy (SOC) for each of the atoms with their spins oriented along the z and x directions. The differences in the energies, $\Delta E_{so} = E^z_{so} - E^x_{so}$, are given in Table 3 (the negative sign marks contribution to uniaxial magnetic anisotropy). For each of the atoms in the compound, we show the largest contribution only, leaving an empty space if that contribution is negligible.

For each of the materials, we can analyze the dominant contributions to MAE. In the case of Ta_3ZnFe_8 (see Table 3), ΔE_{so} of tantalum significantly exceeds that of Fe, as expected from a $5d$-element. If analyzing the d-orbital-resolved difference in SOC energy, one can see (for the details see [20,21]) $d_{x^2-y^2} \rightarrow d_{xy}$ (same spin channel) to be the main source of easy-axis magnetocrystalline anisotropy.

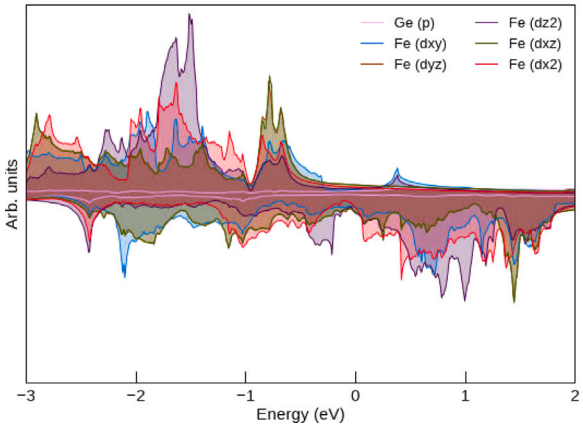

Fig. 7. Spin-polarized DOS (without SOC interaction) of Fe_3Ge. (For interpretation of the references to color in this figure legend, the reader is referred to the web version of this article.)

In Ga_2Fe_6B and $AlFe_2$ we have a mixed contribution to uniaxial MAE from $d_{yz} \rightarrow d_{xz}$ (same spin channel) and $d_{yz} \rightarrow d_{z^2}$ (opposite spin contributions) of the Fe atoms. For Fe_3Ge, $d_{yz} \rightarrow d_{xz}$ (same spin channel) and $d_{x^2-y^2} \rightarrow d_{xy}$ (same spin channel) of Fe are the most important. Finally, uniaxial magnetocrystalline anisotropy of Co_3Ni_2 is defined by cobalt, with the coupling $d_{x^2-y^2} \rightarrow d_{xy}$ (same spin channel) being the dominant one.

The densities of states (DOS) of all five systems are shown in Figs. 6 and 7. In all the materials but Ta_3ZnFe_8, the majority spin channels of

Table 2
Systems from the database with a distance to the convex hull < 50 meV and magnetic moment higher than 1.0 T, with their ground magnetic state, the energy difference between FM and the lowest in energy AFM state (positive sign means the FM state is more stable), saturation magnetization, magnetocrystalline anisotropy, and Curie temperature. NC stands for non-collinear.

Material	Ground state	E_{AFM-FM} meV/at	M_S T	MAE MJ/m^3	T_C K
$Y(Fe_2B)_6$	FM	22	1.15	0.46	
$ZnFe_8Mo_3$	FM	11	0.98	−0.69	
$Zr_2Co_{15}Ni_2$	FM		1.10	−0.02	
$Zr_2Zn_2Co_{15}$	FM		0.96	−0.14	
Ta_3MnFe_8	Ferri		0.83		
Ta_3ZnFe_8	FM	22	0.94	3.02	630
VFe_3Ni_4	FM	59	1.01	0.15	
VFe_8	FM	141	1.85	−0.54	
$VFeCo_6$	FM	39	1.09	−0.05	
$Y_2Al_2Fe_{15}$	FM	54	1.29	0.54	
$Y_2Co_{15}Cu_2$	FM		1.05	−0.19	
$Y_2Co_{15}Ni_2$	FM	14	1.13	−0.10	
$Y_2Cr_2Fe_{15}$	FM	15	1.22	−1.10	
$Y_2Fe_2Co_{15}$	FM	161	1.30	0.01	
$Y_2Ga_2Co_{15}$	FM	98	0.98	−0.11	
$Y_2Mn_2Co_{15}$	FM		1.36	−0.17	
$Y_2Mn_2Fe_{15}$	FM	31	0.96	0.44	
$Y_2V_2Fe_{15}$	FM		1.28	0.35	
$Y_2Zn_2Co_{15}$	FM		0.99	−0.13	
$LiMn_2F_6$	FM	0.8			
Mn_2FeF_6	AFM				
Mn_2GaC	FM	40	0.97	0.49	NC
Mn_2GaNi_3	FM	14	1.34	−0.02	
Mn_2VF_6	AFM				
$MnCoH_4$	FM	37	1.13	−0.33	
$MnFe_2F_6$	AFM				
$MnNb_3Fe_8$	Ferri				
$MnNi_2H_3$	FM	0.6			
Fe_2Co_3Ge	FM	118	1.66	−0.62	
Fe_2CuNi_3	FM	20	1.15	0.16	
Fe_2Ni_2H	FM	18	1.56	−1.26	
Fe_2NiGe	FM	20	1.07	0.33	
Fe_5Co_4	FM	235	2.27	−0.45	
Fe_5Ge	FM	9	1.78	0.17	
Fe_5Ni_4	FM	82	1.79	0.42	
Fe_8Co	FM	157	2.35	−0.11	
Ga_2Fe_6B	FM	136	1.49	0.80	1170
$HfCo_{17}$	FM	122	1.21	0.18	
Al_2Fe_6B	FM	142	1.43	0.18	
$AlFe_2$	FM	138	1.30	1.61	660
Al_2Fe_6Ge	FM	136	1.56	0.51	
Co_3Ni_2	FM	149	1.31	0.89	940
Co_5Ni_3	FM	110	1.37	−0.34	
$CrCoH_4$	AFM				
CrF_2	AFM				
$CrFe_8$	FM	127	1.84	−0.43	
$TaFe_3$	FM	159	1.11	0.21	
$TiFe_3$	FM	139	1.18	−0.04	
$TiFeCo_2$	Ferri	63	0.91		
VFe_2	FM	158	1.05	−0.81	
Mn_2AlGa	FM	44	1.07	−2.08	
Mn_2FeGe	Ferri				
Mn_2ZnGa	FM	80	1.18	−2.00	
Mn_3Ge	Ferri				
Mn_4Ge_2H	FM	4			
$MnFe_2Ge$	FM	11	1.60	0.18	
$MnGaNi_2$	FM	12	1.01	0.30	
$MnVFe_2$	FM	101	1.01	−0.02	
$MnZnH$	FM	34	0.94		
Fe_2CoGe	FM	24	1.29	−0.32	
Fe_2NiGe	FM	21	1.11	0.0001	
Fe_3Ge	FM	139	1.56	1.24	840
Fe_3Si	FM	20	1.10	−0.0001	
$FeCo_2Ge$	FM	73	1.33	0.54	

(*continued on next page*)

Table 2 (*continued*).

Material	Ground state	E_{AFM-FM} meV/at	M_S T	MAE MJ/m^3	T_C K
$FeCo_3$	FM	118	1.93	−0.61	
FeCoH	FM	89	1.69	−0.37	
FeNiH	FM	72	1.37	0.0034	
$GaFe_2Co$	FM	59	1.48	−1.86	
$GaFeCo_2$	FM	108	1.27	0.64	1000
Co_2H	FM	100	1.36	−0.051	
Co_3Ni	FM	132	1.50	−0.37	

Table 3
The difference in SOC energy (VASP) with spin orientation along z and x axis (negative sign corresponds to uniaxial magnetic anisotropy) for the elements of five promising candidates.

Material	ΔE_{so} (1) meV	ΔE_{so} (2) meV	ΔE_{so} (3) meV
Ta_3ZnFe_8	−2.2 (Ta)	−0.024 (Zn)	−0.64 (Fe)
Ga_2Fe_6B	−0.083 (Ga)	−0.43 (Fe)	(B)
$AlFe_2$	−0.013 (Al)	−0.33 (Fe)	
Co_3Ni_2	−0.18 (Co)	−0.052 (Ni)	
Fe_3Ge	−0.34 (Fe)	0.047 (Ge)	

the 3d-states are essentially fully occupied. In Ta_3ZnFe_8, Ta and Fe are considerably hybridized, there are empty states in both spin channels.

Appendix C. Phonon band structures

To investigate the stability of the five promising compounds, we calculated their phonon dispersions and vibrational DOS, see Fig. 8. We can see no unstable phonon modes at the Γ-point and no imaginary frequencies in the phonon dispersion, hence, the materials are dynamically stable. In our investigation, we have not relaxed the structures with respect to the volume or shape changes, however.

Appendix D. Spin-axis dependence of the total energy difference

When calculating MAE at the high-throughput step, we compute it as the difference in total energy between the states with the spins pointing along and perpendicular to the c-axis. However, when the plane formed by the a and b-axes is not perpendicular to the c-axis, additional investigation is required to probe the angular dependence of the total energy.

For all five systems, we calculated the energy change $E^{\theta 2}_{\varphi 2} - E^{\theta 1}_{\varphi 1}$ in the plane formed by a and c-axes, and the plane perpendicular to it, the curves are shown in Figs. 9 and 10.

As we can see, for $AlFe_2$, Co_3Ni_2, Ta_3ZnFe_8, and Fe_3Ge, there is a cosine-like behavior of the energy difference in the a-c-plane with the total energy reaching its maximum when the spins point along the c-axis (Fig. 9). There is almost no change in energy as the spins are rotated in the perpendicular plane. This behavior allows us to conclude, that the systems are characterized by uniaxial magnetocrystalline anisotropy.

Angular behavior of the total energy of Ga_2Fe_6B is different, however. As we rotate the spin axis within the plane perpendicular to a-c (Fig. 10), we can see the cosine-like behavior of the energy difference with the minimum in the b-c-plane. It means that the b-c is the easy plane for the material, while a is the hard axis.

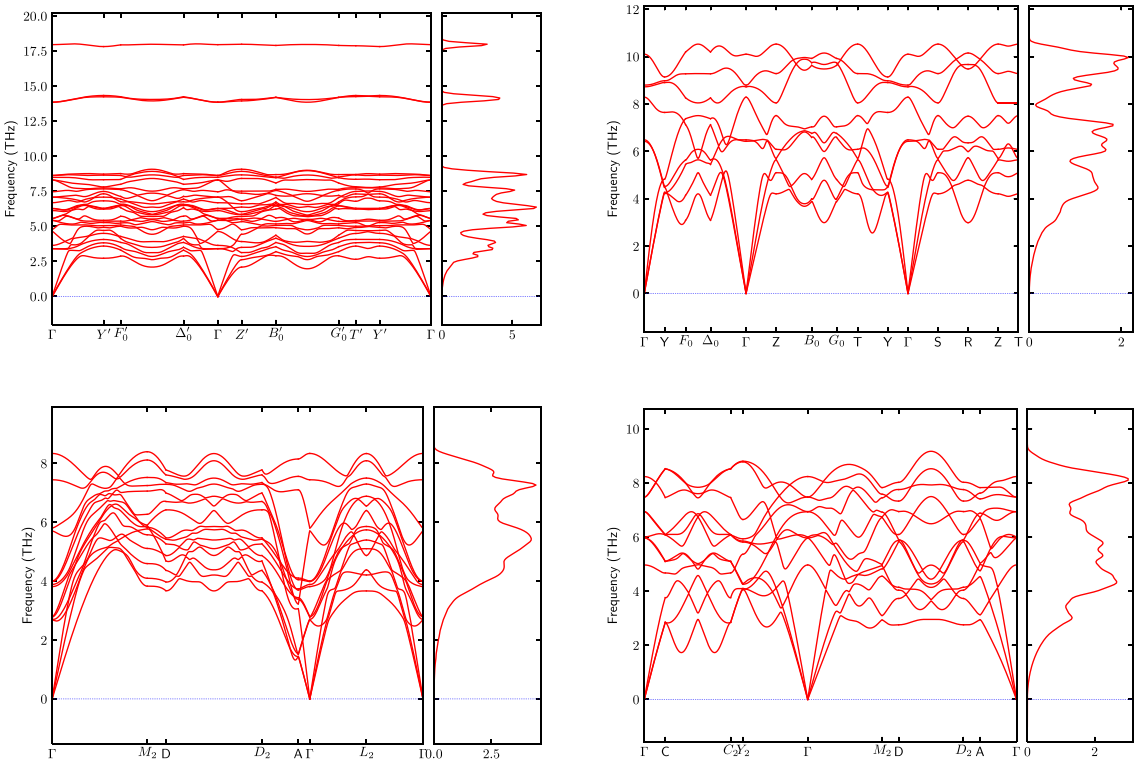

Fig. 8. Phonon dispersions and vibrational densities of states for Ga_2Fe_6B (top left panel), $AlFe_2$ (top right), Co_3Ni_2 (bottom left), and Fe_3Ge (bottom right). (For interpretation of the references to color in this figure legend, the reader is referred to the web version of this article.)

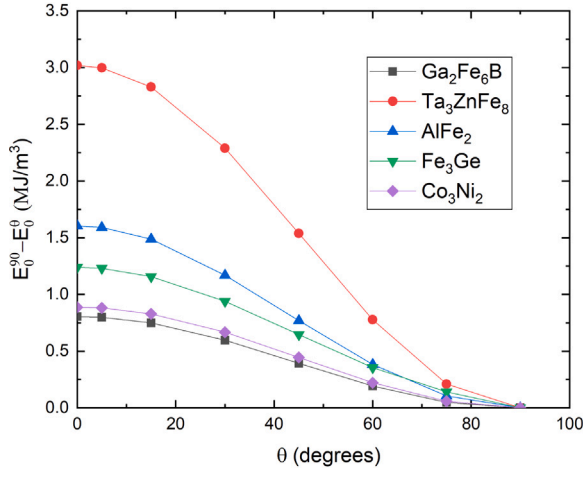

Fig. 9. The difference in total energies $E^{\theta 2}_{\varphi 2} - E^{\theta 1}_{\varphi 1}$ as one of the spin axes is rotated in the plane formed by a and c-axes while the second one is fixed perpendicular to the c-axis. θ and φ are the angles in spherical coordinates. (For interpretation of the references to color in this figure legend, the reader is referred to the web version of this article.)

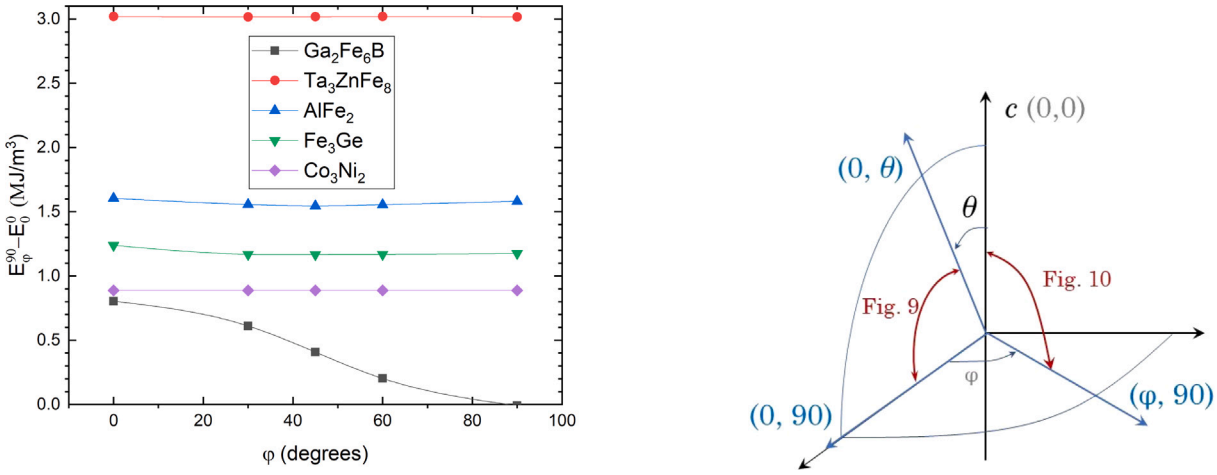

Fig. 10. (a) The difference in total energies $E_{\varphi 2}^{\theta 2} - E_{\varphi 1}^{\theta 1}$ as one of the spin axes is fixed along c and another one is rotated in the plane perpendicular to it. θ and φ are the angles in spherical coordinates. (b) Spin axes orientation for Figs. 9 and 10. (For interpretation of the references to color in this figure legend, the reader is referred to the web version of this article.)

References

[1] R. Skomski, J.M.D. Coey, Permanent Magnetism, Institute of Physics Publishing, Bristol, UK, 1999.

[2] European Commission, Directorate-General for Internal Market, Industry, Entrepreneurship, SMEs, S. Bobba, P. Claudiu, D. Huygens, P. Alves Dias, B. Gawlik, E. Tzimas, D. Wittmer, P. Nuss, M. Grohol, H. Saveyn, F. Buraoui, G. Orveillon, T. Hámor, S. Slavko, F. Mathieux, M. Gislev, C. Torres De Matos, G. Blengini, F. Ardente, D. Blagoeva, E. Garbarino, Report on Critical Raw Materials and the Circular Economy, Publications Office, 2018, http://dx.doi.org/10.2873/167813.

[3] What Is Tesla's Mystery Magnet, https://spectrum.ieee.org/permanent-magnet-tesla.

[4] W. Tang, G. Ouyang, X. Liu, J. Wang, B. Cui, J. Cui, Engineering microstructure to improve coercivity of bulk MnBi magnet, J. Magn. Magn. Mater. 563 (2022) 169912, http://dx.doi.org/10.1016/j.jmmm.2022.169912, URL https://www.sciencedirect.com/science/article/pii/S0304885322007971.

[5] Optimizing composition in MnBi permanent magnet alloys, Acta Mater. 181 (2019) 595–602, http://dx.doi.org/10.1016/j.actamat.2019.10.003.

[6] H. Fang, S. Kontos, J. Ångström, J. Cedervall, P. Svedlindh, K. Gunnarsson, M. Sahlberg, Directly obtained τ-phase MnAl, a high performance magnetic material for permanent magnets, J. Solid State Chem. 237 (2016) 300–306, http://dx.doi.org/10.1016/j.jssc.2016.02.031, URL http://www.sciencedirect.com/science/article/pii/S0022459616300548.

[7] S. Shafeie, H. Fang, D. Hedlund, A. Nyberg, P. Svedlindh, K. Gunnarsson, M. Sahlberg, One step towards MnAl-based permanent magnets - Differences in magnetic, and microstructural properties from an intermediate annealing step during synthesis, J. Solid State Chem. 274 (2019) 229–236, http://dx.doi.org/10.1016/j.jssc.2019.03.035, URL http://www.sciencedirect.com/science/article/pii/S0022459619301458.

[8] X. Zhao, C.-Z. Wang, Y. Yao, K.-M. Ho, Large magnetic anisotropy predicted for rare-earth-free $Fe_{16-x}Co_xN_2$ alloys, Phys. Rev. B 94 (2016) 224424, http://dx.doi.org/10.1103/PhysRevB.94.224424, URL https://link.aps.org/doi/10.1103/PhysRevB.94.224424.

[9] C.A. Bridges, O. Rios, L.F. Allard, H.M. Meyer, A. Huq, Y. Jiang, J.-P. Wang, M.P. Brady, The impact of carbon coating on the synthesis and properties of α-Fe16N2 powders, Phys. Chem. Chem. Phys. 18 (2016) 13010–13017, http://dx.doi.org/10.1039/C6CP00737F.

[10] B. Shen, S. Sun, Chemical synthesis of magnetic nanoparticles for permanent magnet applications, Chem. Eur. J. 26 (30) (2020) 6757–6766, http://dx.doi.org/10.1002/chem.201902916, URL https://chemistry-europe.onlinelibrary.wiley.com/doi/abs/10.1002/chem.201902916.

[11] E. Lottini, A. López-Ortega, G. Bertoni, S. Turner, M. Meledina, G. Van Tendeloo, C. de Julián Fernández, C. Sangregorio, Strongly exchange coupled core|Shell nanoparticles with high magnetic anisotropy: A strategy toward rare-earth-free permanent magnets, Chem. Mater. 28 (12) (2016) 4214.

[12] S. Palaka, M. Yue, Z. Ma, C. Li, H. Li, H. Xu, L. Cong, A facile chemical synthesis of PrCo5 particles with high performance, J. Alloys Compd. 812 (2020) 151674, http://dx.doi.org/10.1016/j.jallcom.2019.151674, URL https://www.sciencedirect.com/science/article/pii/S092583881932907X.

[13] E. Anagnostopoulou, B. Grindi, L.-M. Lacroix, F. Ott, I. Panagiotopoulos, G. Viau, Dense arrays of cobalt nanorods as rare-earth free permanent magnets, Nanoscale 8 (2016) 4020.

[14] T.R. Gao, Y.Q. Wu, S. Fackler, I. Kierzewski, Y. Zhang, A. Mehta, M.J. Kramer, I. Takeuchi, Combinatorial exploration of rare-earth-free permanent magnets: Magnetic and microstructural properties of Fe-Co-W thin films, Appl. Phys. Lett. 102 (2013) 022419.

[15] O. Crisan, F. Vasiliu, A. Crisan, I. Mercioniu, G. Schinteie, A. Leca, Structure and magnetic properties of highly coercive L10 nanocomposite FeMnPt thin films, Mater. Charact. 152 (2019) 245–252, http://dx.doi.org/10.1016/j.matchar.2019.04.028, URL https://www.sciencedirect.com/science/article/pii/S104458031930542X.

[16] J. Lee, G. Lee, T.-Y. Hwang, H.-R. Lim, H.-B. Cho, J. Kim, Y.-H. Choa, Phase- and composition-tunable hard/Soft magnetic nanofibers for high-performance permanent magnet, ACS Appl. Nano Mater. 3 (4) (2020) 3244–3251, http://dx.doi.org/10.1021/acsanm.9b02470.

[17] W. Lei, Y. Yu, W. Yang, M. Feng, H. Li, A general strategy for synthesizing high-coercivity L10-FePt nanoparticles, Nanoscale 9 (2017) 12855–12861, http://dx.doi.org/10.1039/C7NR04849A.

[18] L.H. Lewis, A. Mubarok, E. Poirier, N. Bordeaux, P. Manchanda, A. Kashyap, R. Skomski, J. Goldstein, F.E. Pinkerton, R.K. Mishra, R.C. Kubic Jr., K. Barmak, Inspired by nature: investigating tetrataenite for permanent magnet applications, J. Phys.: Condens. Matter 26 (6) (2014) 064213, http://dx.doi.org/10.1088/0953-8984/26/6/064213.

[19] A. Vishina, O.Y. Vekilova, T. Björkman, A. Bergman, H.C. Herper, O. Eriksson, High-throughput and data-mining approach to predict new rare-earth free permanent magnets, Phys. Rev. B 101 (2020) 094407, http://dx.doi.org/10.1103/PhysRevB.101.094407, URL https://link.aps.org/doi/10.1103/PhysRevB.101.094407.

[20] A. Vishina, D. Hedlund, V. Shtender, E.K. Delczeg-Czirjak, S.R. Larsen, O.Y. Vekilova, S. Huang, L. Vitos, P. Svedlindh, M. Sahlberg, O. Eriksson, H.C. Herper, Data-driven design of a new class of rare-earth free permanent magnets, Acta Mater. 212 (2021) 116913, http://dx.doi.org/10.1016/j.actamat.2021.116913, URL https://www.sciencedirect.com/science/article/pii/S1359645421002937.

[21] A. Vishina, O. Eriksson, H.C. Herper, Fe_2C- and $Mn_2(W/Mo)B_4$-based rare-earth-free permanent magnets as a result of the high-throughput and data-mining search, Mater. Res. Lett. 11 (1) (2023) 76–83, http://dx.doi.org/10.1080/21663831.2022.2117576.

[22] Inorganic Crystal Structure Database, http://www2.fiz-karlsruhe.de/icsd_home.html.

[23] H. Zhou, S. Yan, L. Wu, X. Wan, D. Wang, High-throughput search for potential permanent magnet materials, Phys. Rev. Mater. 7 (2023) 044405, http://dx.doi.org/10.1103/PhysRevMaterials.7.044405, URL https://link.aps.org/doi/10.1103/PhysRevMaterials.7.044405.

[24] C.W. Glass, A.R. Oganov, N. Hansen, USPEX—Evolutionary crystal structure prediction, Comput. Phys. Comm. 175 (11) (2006) 713–720, http://dx.doi.org/10.1016/j.cpc.2006.07.020, URL https://www.sciencedirect.com/science/article/pii/S0010465506002931.

[25] Y. Wang, J. Lv, L. Zhu, Y. Ma, Crystal structure prediction via particle-swarm optimization, Phys. Rev. B 82 (2010) 094116, http://dx.doi.org/10.1103/PhysRevB.82.094116, URL https://link.aps.org/doi/10.1103/PhysRevB.82.094116.

[26] D.C. Lonie, E. Zurek, XtalOpt: An open-source evolutionary algorithm for crystal structure prediction, Comput. Phys. Comm. 182 (2) (2011) 372–387, http://dx.doi.org/10.1016/j.cpc.2010.07.048, URL https://www.sciencedirect.com/science/article/pii/S0010465510003140.

[27] T. Yamashita, N. Sato, H. Kino, T. Miyake, K. Tsuda, T. Oguchi, Crystal structure prediction accelerated by Bayesian optimization, Phys. Rev. Mater. 2 (2018) 013803, http://dx.doi.org/10.1103/PhysRevMaterials.2.013803, URL https://link.aps.org/doi/10.1103/PhysRevMaterials.2.013803.

[28] K. Ryan, J. Lengyel, M. Shatruk, Crystal structure prediction via deep learning, J. Am. Chem. Soc. 140 (32) (2018) 10158–10168, http://dx.doi.org/10.1021/jacs.8b03913, PMID: 29874459.

[29] E.V. Podryabinkin, E.V. Tikhonov, A.V. Shapeev, A.R. Oganov, Accelerating crystal structure prediction by machine-learning interatomic potentials with active learning, Phys. Rev. B 99 (2019) 064114, http://dx.doi.org/10.1103/PhysRevB.99.064114, URL https://link.aps.org/doi/10.1103/PhysRevB.99.064114.

[30] Y. Wang, J. Lv, L. Zhu, Y. Ma, CALYPSO: A method for crystal structure prediction, Comput. Phys. Comm. 183 (10) (2012) 2063–2070, http://dx.doi.org/10.1016/j.cpc.2012.05.008, URL https://www.sciencedirect.com/science/article/pii/S0010465512001762.

[31] J.A. Flores-Livas, Crystal structure prediction of magnetic materials, J. Phys.: Condens. Matter 32 (29) (2020) 294002, http://dx.doi.org/10.1088/1361-648X/ab7e54.

[32] M. Sakurai, R. Wang, T. Liao, C. Zhang, H. Sun, Y. Sun, H. Wang, X. Zhao, S. Wang, B. Balasubramanian, X. Xu, D.J. Sellmyer, V. Antropov, J. Zhang, C.-Z. Wang, K.-M. Ho, J.R. Chelikowsky, Discovering rare-earth-free magnetic materials through the development of a database, Phys. Rev. Mater. 4 (2020) 114408, http://dx.doi.org/10.1103/PhysRevMaterials.4.114408, URL https://link.aps.org/doi/10.1103/PhysRevMaterials.4.114408.

[33] B. Balasubramanian, M. Sakurai, C.-Z. Wang, X. Xu, K.-M. Ho, J.R. Chelikowsky, D.J. Sellmyer, Synergistic computational and experimental discovery of novel magnetic materials, Mol. Syst. Des. Eng. 5 (2020) 1098–1117, http://dx.doi.org/10.1039/D0ME00050G.

[34] W. Xia, M. Sakurai, B. Balasubramanian, T. Liao, R. Wang, C. Zhang, H. Sun, K. Ho, J.R. Chelikowsky, D.J. Sellmyer, C. Wang, Proc. Natl. Acad. Sci. 119 (2022) e2204485119, http://dx.doi.org/10.1073/pnas.2204485119.

[35] T. Liao, W. Xia, M. Sakurai, R. Wang, C. Zhang, H. Sun, K.-M. Ho, C.-Z. Wang, J.R. Chelikowsky, Magnetic iron-cobalt silicides discovered using machine-learning, Phys. Rev. Mater. 7 (2023) 034410, http://dx.doi.org/10.1103/PhysRevMaterials.7.034410, URL https://link.aps.org/doi/10.1103/PhysRevMaterials.7.034410.

[36] J. Schmidt, L. Pettersson, C. Verdozzi, S. Botti, M.A.L. Marques, Crystal graph attention networks for the prediction of stable materials, Sci. Adv. 7 (49) (2021) eabi7948, http://dx.doi.org/10.1126/sciadv.abi7948, URL https://www.science.org/doi/abs/10.1126/sciadv.abi7948.

[37] J. Schmidt, N. Hoffmann, H.-C. Wang, P. Borlido, P.J.M.A. Carriço, T.F.T. Cerqueira, S. Botti, M.A.L. Marques, Large-scale machine-learning-assisted exploration of the whole materials space, arXiv: (2022) 2210.00579, http://dx.doi.org/10.48550/arXiv.2210.00579.

[38] J. Schmidt, N. Hoffmann, H.-C. Wang, P. Borlido, P.J.M. Carriço, T.F.T. Cerqueira, S. Botti, M.A.L. Marques, Large-scale machine-learning-assisted exploration of the whole materials space, Mater. Cloud Arch. (2022) 2022.126, http://dx.doi.org/10.24435/materialscloud:m7-50.

[39] Y. Hinuma, T. Hatakeyama, Y. Kumagai, L.A. Burton, H. Sato, Y. Muraba, S. Iimura, H. Hiramatsu, I. Tanaka, H. Hosono, F. Oba, Discovery of earth-abundant nitride semiconductors by computational screening and high-pressure synthesis, Nature Commun. 7 (2016) 11962, http://dx.doi.org/10.1038/ncomms11962.

[40] Y. Wu, P. Lazic, G. Hautier, K. Persson, G. Ceder, First principles high throughput screening of oxynitrides for water-splitting photocatalysts, Energy Environ. Sci. 6 (2013) 157–168, http://dx.doi.org/10.1039/C2EE23482C.

[41] A. Jain, S.P. Ong, G. Hautier, W. Chen, W.D. Richards, S. Dacek, S. Cholia, D. Gunter, D. Skinner, G. Ceder, K.A. Persson, Commentary: The materials project: A materials genome approach to accelerating materials innovation, APL Mater. 1 (1) (2013) 011002, http://dx.doi.org/10.1063/1.4812323.

[42] P. Villars, H. Okamoto (Eds.), Fe-Ta Binary Phase Diagram 0-0.5 at.% Ta: Datasheet from "PAULING FILE Multinaries Edition – 2022" in SpringerMaterials, Springer-Verlag Berlin Heidelberg & Material Phases Data System (MPDS), Switzerland & National Institute for Materials Science (NIMS), Japan, Copyright 2016 Springer-Verlag Berlin Heidelberg & Material Phases Data System (MPDS), Switzerland & National Institute for Materials Science (NIMS), Japan. URL https://materials.springer.com/isp/phase-diagram/docs/c_0906607.

[43] B. Predel, in: B. Predel (Ed.), Fe - Zn (Iron - Zinc): Datasheet from Landolt-Börnstein - Group IV Physical Chemistry · Volume 12C: "Dy - Er … Ir - Y" in SpringerMaterials, Springer-Verlag Berlin Heidelberg, http://dx.doi.org/10.1007/978-3-642-24778-1_46, Copyright 2013 Springer-Verlag Berlin Heidelberg. URL https://materials.springer.com/lb/docs/sm_lbs_978-3-642-24778-1_46.

[44] G. Balaji Kale, K. Bhanumurthy, S. Parakash Garg, Materials Science International Team, MSIT®, in: G. Effenberg (Ed.), Ta-Zn Binary Phase Diagram Evaluation · Phase diagrams, crystallographic and thermodynamic data: Datasheet from MSI Eureka in SpringerMaterials, MSI Materials Science International Services GmbH, Copyright 2005 MSI Materials Science International Services GmbH. URL https://materials.springer.com/msi/docs/sm_msi_r_20_044054_01.

[45] P. Villars, H. Okamoto (Eds.), Fe-Ga Binary Phase Diagram 10-40 at.% Ga: Datasheet from "PAULING FILE Multinaries Edition – 2022" in SpringerMaterials, Springer-Verlag Berlin Heidelberg & Material Phases Data System (MPDS), Switzerland & National Institute for Materials Science (NIMS), Japan, Copyright 2016 Springer-Verlag Berlin Heidelberg & Material Phases Data System (MPDS), Switzerland & National Institute for Materials Science (NIMS), Japan. URL https://materials.springer.com/isp/phase-diagram/docs/c_0907817.

[46] S. Curtarolo, W. Setyawan, G.L. Hart, M. Jahnatek, R.V. Chepulskii, R.H. Taylor, S. Wang, J. Xue, K. Yang, O. Levy, M.J. Mehl, H.T. Stokes, D.O. Demchenko, D. Morgan, AFLOW: An automatic framework for high-throughput materials discovery, Comput. Mater. Sci. 58 (2012) 218–226, http://dx.doi.org/10.1016/j.commatsci.2012.02.005, URL https://www.sciencedirect.com/science/article/pii/S0927025612000717.

[47] P. Villars, H. Okamoto (Eds.), Co-Ni Binary Phase Diagram 0-100 at.% Ni: Datasheet from "PAULING FILE Multinaries Edition – 2022" in SpringerMaterials, Springer-Verlag Berlin Heidelberg & Material Phases Data System (MPDS), Switzerland & National Institute for Materials Science (NIMS), Japan, Copyright 2016 Springer-Verlag Berlin Heidelberg & Material Phases Data System (MPDS), Switzerland & National Institute for Materials Science (NIMS), Japan. URL https://materials.springer.com/isp/phase-diagram/docs/c_0904886.

[48] F. Albertini, D. Negri, L. Pareti, E.B. Watts, Z. Arnold, J. Kamarad, G. Calestani, A. Deriu, S. Besseghini, Magnetocrystalline anisotropy of Fe_3Ge single crystal: Effect of pressure and Mn substitution for Fe, J. Appl. Phys. 96 (4) (2004) 2110–2114, http://dx.doi.org/10.1063/1.1768613.

[49] K.V. Shanavas, M.A. McGuire, D.S. Parker, Electronic and magnetic properties of Si substituted Fe3Ge, J. Appl. Phys. 118 (12) (2015) http://dx.doi.org/10.1063/1.4931574, 123902.

[50] M. McGuire, K. Shanavas, M. Kesler, P. D.S., Tuning magnetocrystalline anisotropy by cobalt alloying in hexagonal Fe_3Ge_1, Sci. Rep. 8 (2018) 14206, http://dx.doi.org/10.1038/s41598-018-32577-x.

[51] J.M.D. Coey, Rare-earth iron permanent magnets, Springer Series in Solid State Science, Clarendon Press, Oxford, 1996.

[52] G. Kresse, J. Hafner, Ab initio molecular dynamics for liquid metals, Phys. Rev. B 47 (1993) 558.

[53] G. Kresse, J. Furthmüller, Comput. Mat. Sci. 6 (1996) 15.

[54] P.E. Blöchl, Phys. Rev. B 50 (1994) 17953.

[55] J. Perdew, K. Burke, M. Ernzerhof, Phys. Rev. Lett. 77 (1996) 3865.

[56] J.M. Wills, B.R. Cooper, Synthesis of band and model Hamiltonian theory for hybridizing cerium systems, Phys. Rev. B 36 (1987) 3809.

[57] J.M. Wills, M. Alouani, P. Andersson, A. Delin, O. Eriksson, O. Grechnyev, Full-potential electronic structure method, Springer Series in Solid State Science, Springer, Berlin, Germany, 2010.

[58] P.E. Blöchl, O. Jepsen, O.K. Andersen, Phys. Rev. B 49 (1994) 16223.

[59] O. Jepson, O. Anderson, The electronic structure of h.c.p. Ytterbium, Solid State Commun. 9 (20) (1971) 1763–1767, http://dx.doi.org/10.1016/0038-1098(71)90313-9, URL https://www.sciencedirect.com/science/article/pii/0038109871903139.

[60] H.J. Monkhorst, J.D. Pack, Phys. Rev. B 13 (1976) 5188.

[61] O. Eriksson, A. Bergman, L. Bergqvist, J. Hellsvik, Atomistic Spin Dynamics: Foundations and Applications, Oxford University Press, Oxford, 2017.

[62] Y.O. Kvashnin, O. Grånäs, I. Di Marco, M.I. Katsnelson, A.I. Lichtenstein, O. Eriksson, Exchange parameters of strongly correlated materials: Extraction from spin-polarized density functional theory plus dynamical mean-field theory, Phys. Rev. B 91 (2015) 125133, http://dx.doi.org/10.1103/PhysRevB.91.125133, URL https://link.aps.org/doi/10.1103/PhysRevB.91.125133.

[63] A.I. Liechtenstein, M.I. Katsnelson, V.A. Gubanov, Exchange interactions and spin-wave stiffness in ferromagnetic metals, J. Phys. F Metal Phys. 14 (7) (1984) L125–L128, http://dx.doi.org/10.1088/0305-4608/14/7/007.

[64] A. Szilva, Y. Kvashnin, E.A. Stepanov, L. Nordström, O. Eriksson, A.I. Lichtenstein, M.I. Katsnelson, Quantitative theory of magnetic interactions in solids, 2022, http://dx.doi.org/10.48550/ARXIV.2206.02415, URL https://arxiv.org/abs/2206.02415.

[65] R. Skomski, J. Coey, Magnetic anisotropy — How much is enough for a permanent magnet? Scr. Mater. 112 (2016) 3.

[66] A. Togo, I. Tanaka, First principles phonon calculations in materials science, Scr. Mater. 108 (2015) 1–5.

[67] A. Ganose, A. Jackson, D. Scanlon, Command-line tools for plotting and analysis of periodic ab initio calculations, J. Open Source Softw. 3 (28) (2018) 717.

[68] K. Momma, F. Izumi, *VESTA3* for three-dimensional visualization of crystal, volumetric and morphology data, J. Appl. Crystallogr. 44 (6) (2011) 1272–1276, http://dx.doi.org/10.1107/S0021889811038970.

[69] S. Arapan, P. Nieves, H.C. Herper, D. Legut, Computational screening of Fe-Ta hard magnetic phases, Phys. Rev. B 101 (2020) 014426, http://dx.doi.org/10.1103/PhysRevB.101.014426, URL https://link.aps.org/doi/10.1103/PhysRevB.101.014426.

[70] X. Liu, D. Legut, R. Zhang, T. Wang, Y. Fan, Q. Zhang, Tunable magnetic order in transition metal doped, layered, and anisotropic Bi_2O_2Se: Competition between exchange interaction mechanisms, Phys. Rev. B 100 (2019) 054438, http://dx.doi.org/10.1103/PhysRevB.100.054438, URL https://link.aps.org/doi/10.1103/PhysRevB.100.054438.

[71] V. Antropov, L. Ke, D. Åberg, Constituents of magnetic anisotropy and a screening of spin–orbit coupling in solids, Solid State Commun. 194 (2014) 35–38, http://dx.doi.org/10.1016/j.ssc.2014.06.003, URL http://www.sciencedirect.com/science/article/pii/S0038109814002476.

[72] Y. Miura, S. Ozaki, Y. Kuwahara, M. Tsujikawa, K. Abe, M. Shirai, The origin of perpendicular magneto-crystalline anisotropy in L10–FeNi under tetragonal distortion, J. Phys.: Condens. Matter 25 (10) (2013) 106005, http://dx.doi.org/10.1088/0953-8984/25/10/106005.

[73] L. Ke, M. van Schilfgaarde, Band-filling effect on magnetic anisotropy using a Green's function method, Phys. Rev. B 92 (2015) 014423, http://dx.doi.org/10.1103/PhysRevB.92.014423, URL https://link.aps.org/doi/10.1103/PhysRevB.92.014423.

[74] J. Zhang, B. Yang, H. Zheng, X. Han, Y. Yan, Large magnetic anisotropy and strain induced enhancement of magnetic anisotropy in monolayer TaTe2, Phys. Chem. Chem. Phys. 19 (2017) 24341–24347, http://dx.doi.org/10.1039/C7CP04445C.